RSC Advances

COMMUNICATION

View Article Online
View Journal | View Issue

Cite this: *RSC Adv.*, 2015, **5**, 13175

Multispectral Bayesian reconstruction technique for real-time two color fluorescence microscopy

Shilpa Dilipkumar,†[a] Ravi Manjithaya†[b] and Partha Pratim Mondal†*[a]

Received 25th November 2014
Accepted 14th January 2015

DOI: 10.1039/c4ra15225e

www.rsc.org/advances

We have developed a real-time imaging method for two-color widefield fluorescence microscopy using a combined approach that integrates multi-spectral imaging and Bayesian image reconstruction technique. To enable simultaneous observation of two dyes (primary and secondary), we exploit their spectral properties that allow parallel recording in both the channels. The key advantage of this technique is the use of a single wavelength of light to excite both the primary dye and the secondary dye. The primary and secondary dyes respectively give rise to fluorescence and bleed-through signal, which after normalization were merged to obtain two-color 3D images. To realize real-time imaging, we employed maximum likelihood (ML) and maximum *a posteriori* (MAP) techniques on a high-performance computing platform (GPU). The results show two-fold improvement in contrast while the signal-to-background ratio (SBR) is improved by a factor of 4. We report a speed boost of 52 and 350 for 2D and 3D images respectively. Using this system, we have studied the real-time protein aggregation in yeast cells and HeLa cells that exhibits dot-like protein distribution. The proposed technique has the ability to temporally resolve rapidly occurring biological events.

One of the key hindrances for real-time high-quality imaging in fluorescence microscopy is the slow rate of data acquisition, processing and potential bleed-through signal.[1,2] While bleed-through cause optical artifacts that potentially hampers the image quality, one can think of alternate route to utilize this signal for high resolution two-color fluorescence microscopy. This enables parallel acquisition of fluorescence and bleed-through signal. Although we demonstrate the technique on a widefield system, the proposed technique can be extended for real-time imaging in two-color version of TIRF,[3] STED[4] and structured illumination[6] microscopy. A number of biophysical studies have benefited from the two-color fluorescence microscopy.[7] For example, it is observed that, detection and accurate quantification of the presence of duplex DNA or RNA play vital role for the protein synthesis.[8] Similarly, chromophore based dual-color switchable nanoparticles and polymer nanoparticles have shown much promise by alternately emitting two distinct colors which can be an efficient tool for high-resolution cell imaging.[9,10] Spectroscopic analysis suggests that PATagRFP photoactivable protein as an excellent protein tag for two-color imaging techniques including, PALM[5] and its variants (sptPALM).[11] Of-late, there has been an increased study in the field of cell biology and biomedical physics. Some of the interesting studies include tumor cell targeting using bleomycin (BLM) that show dye-labelled BML as a potential candidate for targeting cancer cell and human breast carcinoma cells.[12,13] In another study, reduction of cell metabolic activity, induction of cell cycle arrest and disruption of mitotic spindle was observed when cells were exposed to multi-wall CNTs.[14,15] There are many more biological studies and applications that need fast two-color 3D fluorescence imaging.

For constructing two-color image of the biological specimen, existing techniques acquire multiple scans sequentially from two separate channels and merge the images (obtained from multiple channels). These imaging systems are quite cumbersome and expensive as they employ multiple laser lines. So, a technique that enables two-color imaging using a single laser line is highly desirable. Further, this will circumvent the need for two laser lines for two-color fluorescence imaging. Note that, existing two-color imaging techniques have many limitations such as: (1) poor temporal resolution, since this requires changing channels, switching excitation sources and emission filters, (2) spectral overlap and (3) artifact-prone images. All these factors limit the speed of data acquisition, degrade image quality and hence are not capable of studying rapidly occurring biological events. However, researchers have recently studied few dynamic events in biological systems using high cost

[a]*Nanobioimaging Laboratory, Department of Instrumentation and Applied Physics, Indian Institute of Science, Bangalore 560012, India. E-mail: partha@iap.iisc.ernet.in*
[b]*Molecular Biology and Genetics Unit, Jawaharlal Nehru Center for Advanced Scientific Research, Bangalore 560064, India*

† PPM and SD conceived and designed the study. SD, RM and PPM performed the experiments whereas, computational studies were carried out by SD. The samples were prepared by SD and RM. SD, PPM and RM analyzed the data, produced the figures and wrote the manuscript.

dedicated imaging systems. For example, Liu *et al.*, used a two-color stimulated emission depletion (STED) microscope to show that, Rab3-interacting molecule (RIM) binding protein is essential for rapid release of neurotransmitter.[16] In another study, it is observed that, Ca^{2+} ions get released at a much faster rate (about, 100 ms) during muscle contraction.[17] Protein folding is believed to be one of the fastest biological processes that has several consequences ranging from transcription to migration. This generally occurs at an incredibly fast rate ranging from few hundred nano-seconds to tens of micro-seconds.[18,19] Fast processes are also observed in plants where directed Golgi units move at a speed of few-tens of microns.[20] Recently, the dynamics of tubulin and kinesin has been observed in living (*Drosophila melanogaster*) S2 cells using high-speed structured illumination microscopy.[21] Simultaneous visualization of various organelles and subcellular constituents including supramolecular structures such as protein complexes are routinely carried out to spatially and temporally establish their relative occurrences within the cell. There are several other biochemical processes that can be probed by real-time two-color imaging system. Therefore, real-time imaging of intracellular components in a cell is of pivotal importance for understanding its behavior. An alternate way to achieve real-time imaging is to use fast computing engines.[22] Here, we present a multi-spectral microscopy approach to identify and take advantage of the signal caused by bleed-through for real-time two color fluorescence imaging. The potential advantage of the proposed technique with respect to the existing techniques are many. This include, (1) single source excitation, (2) parallel data acquisition in both the channels, (3) GPU based CUDA computing engines for rapid two-color imaging. Accordingly, we have integrated optical system with fast computing engines, with the aim of obtaining high quality 3D images in real-time.

Results

The schematic diagram of the proposed imaging system is shown in Fig. 1. Fluorescent beads (Invitrogen, P7220) of diameter 0.175 $\pm$ 0.005 μm were used for both calibration and for demonstrating the proposed two-color imaging technique (Fig. 1). Two different colored nanobeads ($\lambda_{exc}|\lambda_{emi}$: 505 nm|515 nm and 540 nm|560 nm) are combined and imaged. The primary and the bleed-through signals from the nanobeads are shown as the green and red circles, respectively (Fig. 2A). The merged image obtained using the proposed technique is shown in Fig. 2B, whereas, Fig. 2C demonstrates the bleed-through mechanism for the nanobeads sample. The spectra (obtained from the USB4000 spectrometer (Ocean Optics)) clearly shows two prominent emission peaks, one at 515 nm and the bleed-through signal at 560 nm for an excitation wavelength of 488 nm.

In this context, to follow the protein aggregation in real time, we use *S. cerevisiae* cells where HTT gene (codes for Huntingtin gene) and Ape1 gene (codes for amino peptidase-I, a vacuolar hydrolase) were expressed respectively as GFP and RFP fusion protein.[23–25] As observed in Fig. 3B, both the protein aggregates show two separate dot-like distribution pattern around the vacuoles of yeast cell. Therefore simultaneous acquisition of images for both the aggregates provide spatial understanding of their distribution within the cell. GFP and RFP has an excitation maxima at 488 nm and 555 nm respectively and they emit at 509 nm and 584 nm, respectively. The fluorescence from GFP and RFP are simultaneously acquired using detector array (D1 and D2). Camera 1 captures the signal from the primary channel (GFP) and camera 2 captures the bleed-through (RFP) signal. GFP and RFP are shown as green and red circles, respectively in Fig. 3A. Fig. 3C corresponds to the spectral signature with two peaks, one at 509 nm (primary signal) and the other at 584 nm (bleed-through signal), when the specimen is excited at 488 nm. Huntingtin protein aggregates can be seen as discrete foci with varying size (see, Fig. 3B). Interestingly using the bleed through signal, we were able to clearly detect a perivascular dot representing Ape1 RFP protein aggregates. The HTT aggregates did not appear to colocalize with Ape1 suggesting that the two aggregates were distinct entities. As the Ape1 marks the site for autophagosome biogenesis (Pre-autophagosomal structure, PAS), further studies may shed light on the effect of HTT aggregates on PAS formation and autophagy function. Thus localization of HTT aggregates with respect to PAS may enable better understanding of the relationship between protein aggregates and the role of autophagy in clearing them.

To further enhance the performance of the proposed technique and enabling real-time imaging of large datasets, we employ statistical techniques (maximum likelihood (ML) and maximum *a posteriori* (MAP)) for 3D image reconstruction. We choose BPAE cell lines (F-actin labelled with Alexa Fluor 488 and mitochondria labeled with Mitotracker CMXRos Red) as shown in Fig. 4. The images are acquired using a single wavelength of light (488 nm) to capture fluorescence from two fluorescent probes. As shown in Fig. 4, the F-actin images (green channel) corresponds to the primary signal and the bleed-through signal (red channel) comes from the mitochondria. The primary image and the bleed-through signal were merged to obtain two-color image in real-time. Reconstruction show suppression of noise and reduction of artifact in real-time.[22,26–28,32] Moreover, we employed CUDA based FPGA computing engine to realize real-time imaging. Notably, 2D reconstructed images require 38 ms whereas CPU require 2 s to execute. The corresponding ML and MAP reconstructed images of F-actin and mitochondria are shown in Fig. 4B and C, respectively. The reconstructed images show substantial reduction in background noise and simultaneously preserves minute features. The proposed setup captures significant bleed-through signal using dedicated D2 camera and hence the mitochondrial structure is clearly visible. Further, reconstruction of the raw images from the proposed setup enhances the signal-to-background (SBR) ratio and hence the features are better resolved whereas, Fig. 4D shows the SBR level comparison for the raw image and reconstructed images (ML and MAP) for both the green and red channels. The SBR of ML and MAP reconstructed images show an improvement of approximately 4 times when compared to the raw image. It can be clearly seen that the reconstructed images significantly reduce the noise level in the acquired images, thus further

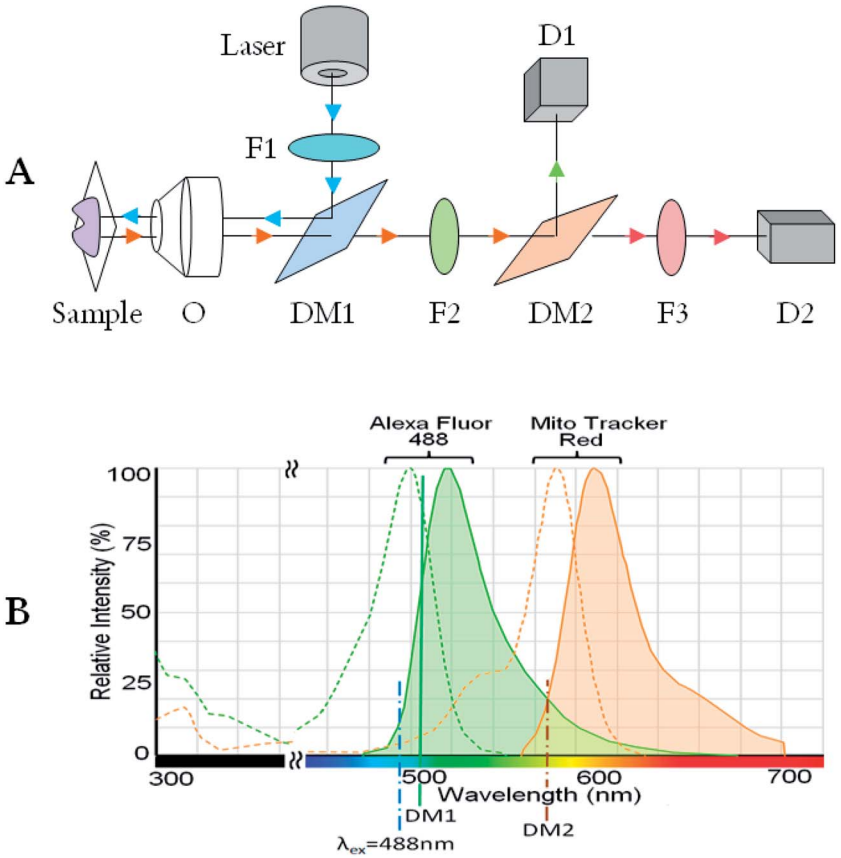

Fig. 1 (A) Schematic representation of the proposed optical setup (widefield system), (B) the spectra demonstrating bleed-through mechanism using Invitrogen online tool.

enhancing the quality of the two-color images. Corresponding intensity profile plots on the images acquired in both the channels (F-actin and mitochondria) and reconstructed images are shown in Fig. 4E and F, respectively. The intensity plots (indicated by white line in Fig. 4) demonstrate significant SBR improvement in the reconstructed images.

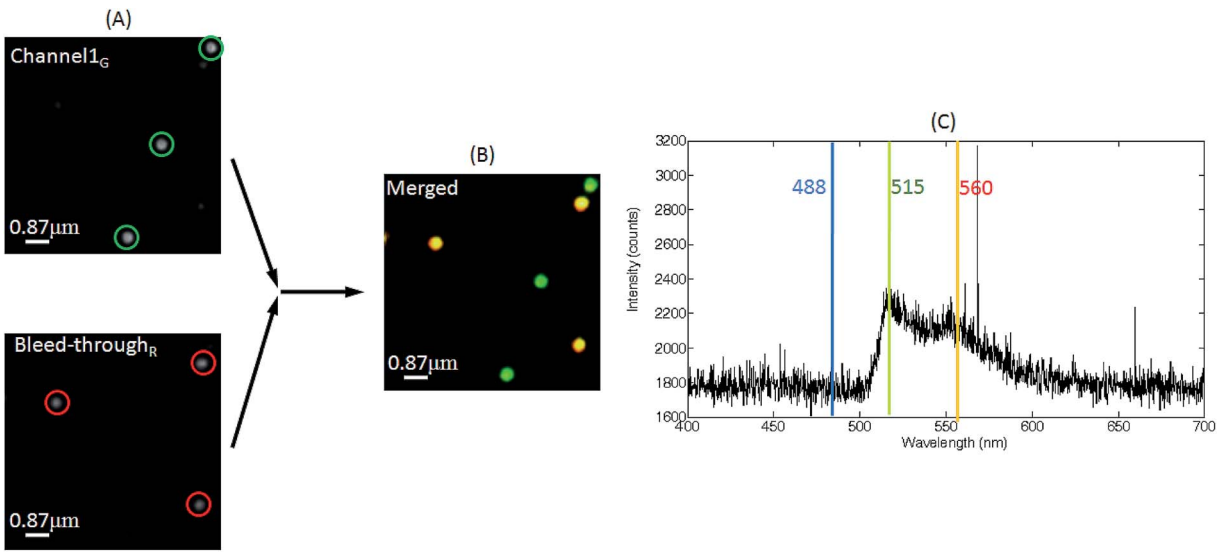

Fig. 2 (A) Green and orange nanobeads imaged by simultaneously capturing the primary channel signal (green circle) and the bleed-through (red circle) with the proposed widefield system. (B) Two-color image obtained by merging the green and red channel images obtained simultaneously from both the channels. (C) Spectra obtained from the spectrometer, shows two peaks at 515 nm and 560 nm.

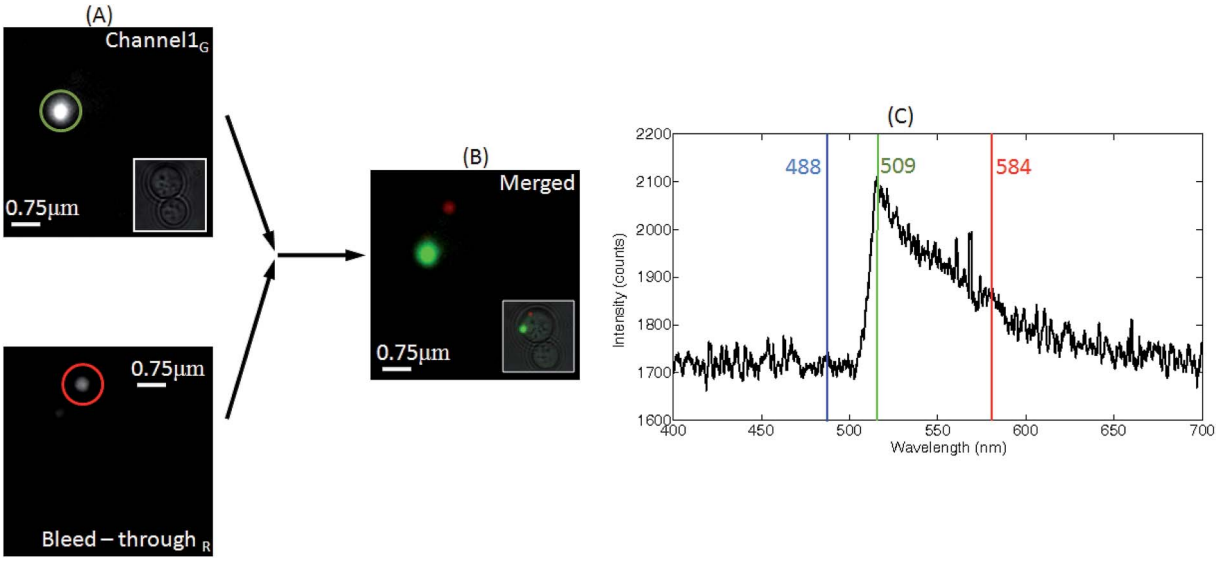

Fig. 3 (A) Green Fluorescent Protein (GFP) and Red Fluorescent Protein (RFP) imaged simultaneously by capturing the signal from green and red (bleed-through) channel in the proposed widefield system. The inset shows the transmission mode image of the *Saccharomyces cerevisiae* (yeast) cells. (B) Signal from both the channels (green and red) are merged in real-time. Inset shows the fluorescent signals overlaid on the transmission image. (C) Spectrum obtained from the spectrometer, clearly showing two peaks at 509 nm and 584 nm.

Next, we studied the protein aggregation in HeLa cells which occurs due to the over production of glutamate residues that are common in neurodegenerative diseases including, Huntington disease.[29–31] We have chosen to work on a grid size of 128 × 128 × 47 which is equivalent to a volume of 3622 μm^3. It is found that, CUDA-GPU (2496 cores) based 3D volume reconstructed images require 79 ms whereas CPU (3 cores) based implementation require 34 s to execute ML method. On the other hand, MAP-reconstruction takes approximately 102 ms on GPU and 36 s on CPU. Both raw and real time reconstructed images (ML and MAP) are shown in Fig. 5. The two-color reconstructed 3D data reveals discrete localization of Huntingtin proteins (Htt74Q) (see, white arrow) in different layers of HeLa cells (see, slices number 17, 21, 26, 33, 35 in Fig. 5). Real-time ML and MAP reconstructions give better visualization (high contrast and low noise) of 3D cell along with improved localization of proteins (green dots) as seen in Fig. 5. Specifically, two different MAP based techniques were employed based on the potential function (Quadratic and Median-Filter) to suppress the random noise. The overall contrast of the reconstructed ML and MAP images are approximately enhanced by 1.96 and 1.79 times, respectively. The details of these techniques can be found in ref. 22, 27 and 32. One can observe the protein aggregates of varying sizes. In HeLa cells, the plasmid DNA containing 74 glutamine repeats of Htt protein conjugated with EGFP (c-terminally tagged) forms medium sized aggregates of about 2 to 3 in numbers per cell as seen in Fig. 5 (circles and arrows). Thus, the study quantizes the real-time protein aggregation in HeLa cells.

Discussions

In cell biology and applied physics, two-color fluorescence imaging is an indispensable tool. Using fluorescence microscopy, many biological studies have been successfully carried out which include, protein dynamics,[33] neuron-tracing[34] and protein interaction.[35] Here, we propose a real-time version of two-color high-resolution fluorescence microscopy system for studying dynamical biological processes. Such an imaging system may pave the way for high-resolution two-color imaging of cellular organelles in real-time.

In the proposed approach, two dyes were suitably chosen based on their spectral overlap (≈10%) and using an appropriate filter bank (in the detector sub-system), the signals were separated. The resulting single color 3D images (obtained from respective channels) were merged in real-time to construct two-color 3D images. Judicious selection of the dyes and utilization of the bleed-through signal is essential for the technique to succeed. The photo-chemical mechanism behind the technique works on the fact that, both the primary and secondary dyes are excitable with a single wavelength of light. Due to the parallel nature of image acquisition in both the channels, the technique is fast and improves temporal resolution. Subsequently, we subjected the data (obtained from each channel) directly to the state-of-art GPU based fast computing engine. The goal is to process the noisy and optically-aberrated data in real-time, so as to generate high-resolution 3D image in real-time. Statistical reconstruction techniques such as, ML and MAP were appropriately implemented on FPGA computing engines to enable rapid computation of key steps (convolution involving 3D FFT, 3D IFFT, point-by-point division *etc.*) involved in the reconstruction process. The results show an impressive 79 ms execution of 3D volume data (128 × 128 × 47 pixels). We found that, the execution time increases dramatically for large-size images. Therefore, we conclude that, real-time 3D imaging can at best be obtained for a maximum data processing rate of

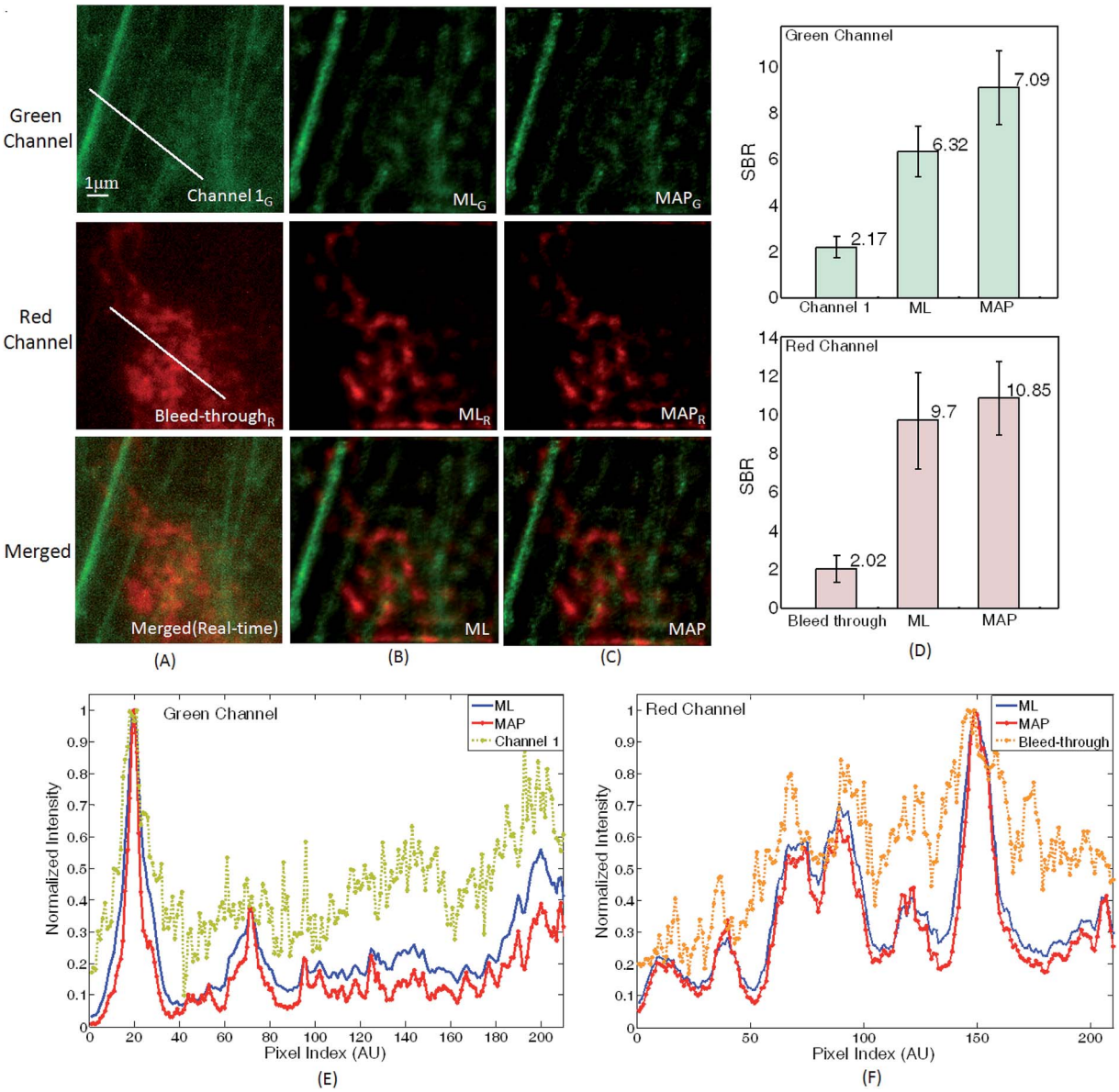

Fig. 4 Visualization of F-actin filaments and mitochondrial network of BPAE cells using the proposed widefield system. (A) Images from the primary green channel, bleed-through from the red channel and real-time merged image of the two channels (pseudo-colors added). (B) ML reconstructed image, (C) MAP reconstructed image, (D) signal-to-background comparison for green channel and the red (bleed-through) channel. (E) and (F) respectively show the intensity profile plots for raw, ML, MAP and color camera image (green and red components).

3 MB s^{-1}. In future, this restriction can be lifted by using computing engines with large number of cores and multiple GPUs. A combined multispectral technique seems to be a promising approach for understanding complex biological events.

The proposed technique has key advantage over the existing sequential scanning technique. The existing two-color fluorescence imaging techniques involve sequential excitation of dyes followed by merging so as to obtain two color image. This has the following limitations: (1) the technique requires sequential scanning process that consumes the precious imaging time and thereby not suitable for two-color imaging of rapidly occurring biological events,[13,16] (2) not a real time imaging modality since it requires large post-processing time for obtaining high quality images, and (3) involves frequent changing of filter-sets. On the other hand, the proposed technique overcomes these limitations by simply diverting the respective signals (fluorescence and bleed-through) to the respective detectors and subsequently to the CUDA computing system. So, the sequential scanning is avoided and the data is acquired in-parallel and processed by the parallel computing engine, thereby enabling real-time imaging. The statistical techniques such as, ML and MAP ensures high quality reconstruction. It may however, be noted that one can achieve data acquisition by employing two lasers as well and, use a filter and an image splitter to image two

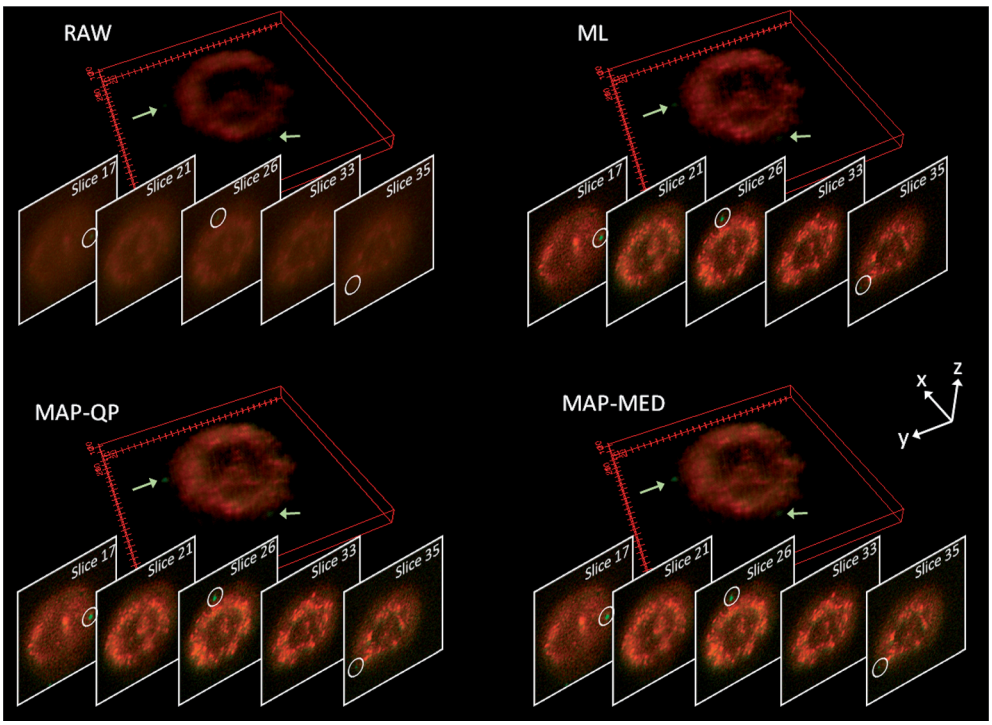

Fig. 5 Observation of Huntingtin protein aggregation in HeLa cells using the proposed widefield system. 3D visualization of real-time two-color raw images obtained using the proposed technique. Both the fluorescence and bleed-through signals were collected to reconstruct the 3D image. Fast computing engines (Tesla K20 GPU system with 2496 cores) were employed for real-time ML and MAP reconstruction of 3D images. For better 3D visualization, we have shown slices 14–47 of the cell. Specifically, slice number 17, 26, 35 were shown that illustrate the dynamic protein aggregation process (represented by, arrows and circles) in a single HeLa cell. ML and MAP reconstruction show better visualization of the underlying mitochondrial network (see, slice numbers, 21 and 33).

colors simultaneously. Proposed technique take advantage of bleed-through signal to render two-color images. However, this technique is better suited for imaging biological specimens where bleed-through is strong and gives information about the process under study.

Since the excitation efficiency of the primary dye is stronger than that of secondary dye, this requires normalization and boosting the signal-to-noise ratio (SNR) before merging them.[28,32,36–38] To achieve this, we employed real-time ML and MAP techniques. The results (Fig. 2–4) indicate that, the process is efficient and is capable of producing quality images for real-time two-color fluorescence microscopy.

Unlike existing techniques, the proposed technique employs a single laser to render two-color imaging. This enables parallel data acquisition in both the channels. When coupled with fast ML and MAP reconstruction techniques, this technique leads to real-time 3D two-color fluorescence imaging. Specifically, the integration of CUDA based fast computing engines facilitates super-fast processing of two-color 3D data. This greatly simplifies the existing state-of-art two-color imaging systems that require two laser lines. Future techniques may see parallel data acquisition from more than two channels and real-time processing with even faster computing engines. This technique may have immediate applications in biomedical imaging, medical physics and clinical health-care.

Methods

Bleed-through mechanism

In this article, we utilize bleed-through signal for high resolution two-color fluorescence microscopy. In general, there are three primary ways that can potentially result in fluorescence bleed-through or cross-talk as far as two-color imaging is concerned. First occurs due to the overlap between the emission spectra of primary and secondary fluorophores. This happens in-general because emission spectra has long tails resulting in cross-emission. Second, the emission from one fluorophore results in the excitation of another fluorophore where the fluorophores lie within few nanometers distance. This generally results in FRET effect. Third, cross-excitation of two different fluorophores in which the excitation wavelength lies well-within the excitation spectra of both the fluorophores. Here, we deal with the third case for enabling real-time two-color fluorescence imaging.

The fact that a fluorophore can be excited anywhere within the excitation spectra and not necessarily at its peak, can be utilized for real-time two-color fluorescence imaging. The excitation of both the primary and secondary fluorophores can be chosen such that, the primary fluorophore is excited at the peak of its excitation spectra and secondary fluorophore is excited at the tail of its excitation spectra. We have chosen two fluorophores: Alexa Fluor-488 and MitoTracker CMXRos Red. Alexa

Fluor-488 has an excitation maximum at 488 nm while, MitoTracker Red has an excitation maximum at 565 nm, but it can also be excited at the tail of its excitation spectra with low efficiency using 488 nm wavelength light. We have used a single excitation source of wavelength 488 nm to excite both the fluorophores. So, there is natural bleed-through from secondary fluorophore (MitoTracker Red). With an appropriate optical arrangement using filters and dichroic mirror assembly, we separated the signals (fluorescence and bleed-through) from the specimen at the detection sub-system. This enabled simultaneous detection of photons emitted by both the fluorophores.

Two-color fluorescence imaging system

The optical setup along with the photo-chemical mechanism which demonstrates the proposed two-color fluorescence microscope is shown in Fig. 1. Randomly polarized light from the laser is filtered by the excitation filter F1 and subsequently directed to the sample by the dichoroic mirror DM1 and the objective O. The emitted fluorescence is then captured by the same objective lens and then transmitted through the dichroic mirror DM1 (DM 505, Thorlabs). The emission filter F2 (BA 510, Thorlabs) placed in the detection arm ensures that all wavelengths above the specified cutoff (510 nm) pass through. A second dichroic mirror DM2 (DM 567, Thorlabs) is placed in the detection path to separate the two signals emitted by the primary and secondary fluorophores. Both the signals are simultaneously collected at the detectors D1 and D2 (Chameleon cameras CMLN-13S2M, Pointgrey). A long-pass filter F3 (FEL 550) is introduced into the red channel to further ensure that any wavelength less than 550 nm does not reach the detector D2. This ensures efficient collection of light emitted by the secondary fluorophore. Finally, the data obtained from both the detectors are normalized and merged in real-time.

The mechanism which enables real-time two-color fluorescence imaging using bleed-through signal is shown in Fig. 1B. The excitation spectra of both the fluorophores indicate that they are excitable at 488 nm. The primary fluorophore (Alexa Fluor 488) is excited at 100% by the incident light and the secondary fluorophore (MitoTracker Red) is excited at 10% of its excitation maxima. The emission spectra from F-actin filaments (tagged with primary dye, Alexa Fluor 488) and a relatively weak bleed-through signal from mitochondrial network (tagged with MitoTracker Red) is collected. The emission maxima occurs at 520 nm and 585 nm, respectively for Alexa Fluor 488 and MitoTracker CMXRos Red fluorophores. The distinct collection of the emission from individual fluorophores is accomplished by using the dichroic mirror DM2 (with a cut-off of $\lambda_c = 567$ nm). Both the signals are normalized before merging them in real-time.

Sample preparation

Materials. All the optical components used for the experimental setup was acquired from Thorlabs. The CMOS Chameleon cameras (CMLN-13S2M) were obtained from Pointgrey. The 100×, 0.6–1.3 variable NA objective lens was procured from Olympus. The yellow-green and orange fluorescent nanobeads (P7220) were purchased from Invitrogen and Agar powder was acquired from Sd Fine Chemicals. Htt 103Q-GFP was procured from Addgene (pRS 416-Htt103Q GFP). Ape1-RFP was the kind gift of Michael Thumm (Gottingen Graduate School for Neurosciences, Germany).

Preparation of two-color nanobeads sample. To prepare the nanobeads gel sample, 100 mg of Agar powder was added to 100 ml distilled water. The solution was heated at 100 °C for 10 minutes. Once the molten solution is ready, 5 μl each of yellow-green (505/515) and orange (540/560) were added to 1 ml of agar solution with intense stirring. 200 μl of the agar-nanobeads solution is pipetted out on a clean coverslip and allowed to solidify at room temperature and images are acquired under the microscope.

Preparation of GFP and RFP tagged yeast cells. 10 ml *Saccharomyces cerevisiae* was inoculated and incubated with overnight shaking at 30 °C. The overnight culture was counted and 50 ml of warm Yeast Extract–Peptone–Dextrose plus Adenine medium (YPAD) was inoculated to a cell density of 5×10^6 ml culture. The culture was incubated at 30 °C on a shaker at 200 rpm until it is equivalent to 2×10^7 cells per ml. The culture was harvested in a sterile 50 ml centrifuge tube at $3000 \times g$ (5000 rpm) for 5 min. The medium was then poured off and the cells were resuspended in 25 ml of sterile water and centrifuged again. The water was poured off again and the cells were resuspended in 1.0 ml of 100 mM lithium acetate (LiAc) and the suspension was transferred to a 1.5 ml microfuge tube. The cells were pelleted at top speed for 15 s and LiAc was removed with a micropipette. The cells (2×10^9 cells per ml) were resuspended to a final volume of 500 μl of 100 nM LiAc. 1.0 ml sample of single-stranded DNA (SS-DNA) was boiled for 5 minutes and quickly chilled in ice water. The cell suspension was vortexed and 50 μl samples were pipetted into labeled microfuge tubes. Cells were pelleted and the LiAc was removed with a micropipette. The basic 'transformation mix' consists of: 240 μl PEG (50% w/v), 36 l 1.0 M LiAc, 50 μl SS-DNA (2.0 mg per ml), x μl plasmid DNA (0.1–10 μg) and $34x$ μl sterile ddH_2O. These ingredients were added carefully in the same order and vortexed vigorously for about 1 minute until the cell pellet has been completely mixed. This is then incubated at 30 °C for 30 minutes, followed by heat shock in a water bath at 42 °C for 30 minutes. The tubes were then microfuged at 8000 rpm for 15 s and the transformation mix was removed with a micropipette. 1.0 ml of sterile water was pipette into each tube and the pellet was resuspended by pipetting it up and down gently. Place 200 μl of the transformation mix onto SC-minus plates. Plates were incubated at 30 °C for 3 days. Positive colonies were identified by microscopy. For imaging experiments, *S. cerevisiae* strain (BY4741 mRFP-APEI::HIS, HTT 103Q-GFP::URA) were grown in defined synthetic dextrose medium without uracil and histidine (SD-URA-HIS). To obtain a monolayer of cells, 3–4 μl of actively growing culture was sandwiched between coverslip and a 2% agarose pad placed on a slide.

Transfection of HeLa cell with Htt94Q and MitoTracker staining. HeLa cells were cultured in growth medium containing DMEM (Sigma) and 10% Foetal bovine serum (PAN biotech GmbH) at 37 °C, supplemented with 5% CO_2. For transfection

8×10^5 cells were seeded on a 60 mm dish and allowed to attach for 24 h. Transfection of pEGFP-Htt74Q (Addgene) was performed using Lipofectamine 2000 (Invitrogen) as per manufacturer's instruction. Expression of EGFP containing mutant Huntingtin (Htt74Q) a protein known to aggregate upon expression and localize nonspecifically in the cell was observed under fluorescent microscope (Delta Vision) 48 h post transfection. To stain mitochondria, MitoTracker Orange (Invitrogen) was used as advised by manufacturer's instruction. Briefly, EGFP-Htt74Q expressing cells were treated with warm growth medium containing 1 μM MitoTracker Orange for 10 min. Cells were washed three times with PBS to remove excess dye and detached using 1× trypsin.

TESLA-K20 with CUDA

The iterative ML and MAP reconstruction techniques are implemented using Nvidia Tesla-K20 graphics processing unit (GPU) with Compute Unified Device Architecture (CUDA – Version 5.5) parallel computing platform. Tesla-K20 runs at 2.6 GHz with a total board memory of 5 GB. It has 2496 cores, with 20 128M × 16 GDDR5 SDRAM and processor core clock speed of 706 MHz. This facilitates the multithreading and parallel processing of 3D data generated by proposed two-color imaging system. Compared to CPU based system, GPU performs complex mathematical operations within a few tens of milliseconds thereby making it suitable for real-time imaging. The reference CPU is a 3.06 GHz Intel Core i3 system with 3.99 GB RAM. The algorithms have been implemented on the fast computing engines using CUDA C. The reconstruction techniques involve computationally intensive operations like 3D FFT, 3D inverse FFT, point-to-point multiplication and point-to-point division of large volumes of data. Nvidia CUFFT library handles the 3D FFT and IFFT implementations.

Conflict of Interest

The authors declare no competing financial interests.

Acknowledgements

All the authors contribute equally to this work. PPM would like to thank Department of Science and Technology, BRNS (DAE) and Indian National Science Academy for financial support. RM would like to acknowledge India Alliance. The authors would like to thank Prof. Michael Thumm (Georg-August-Universitat Gottingen, Germany), Susan Lindquist (Whitehead Institute for Biomedical Research, Massachusetts Institute of Technology, Cambridge, USA) for plasmids, Aravinda Chavalamane (JNCASR, Bangalore, India) for HeLa cells and S. N. Suresh (JNCASR, Bangalore, India) for technical help. We thank Dr Latha Kumari (FIU, Florida, USA) and Dr Subhra Mandal (Radboud University Nijmegen Medical Centre, Nijmegen, Netherlands) for going through the entire manuscript. We acknowledge support from Prof. K. Rajan (Physics, Indian Institute of Science) for CUDA based FPGA implementation and Dr Ambarish Ghosh for the color cameras.

References

1 J. Chena, R. V. Dalal, A. N. Petrov, A. Tsaia, S. E. O. Leary, K. Chapin, J. Cheng, M. Ewan, P. L. Hsiung, P. Lundquist, S. W. Turner, D. R. Hsu and J. D. Puglisi, *Proc. Natl. Acad. Sci. U. S. A.*, 2014, **111**, 664669.
2 D. I. Cattoni, J. B. Fiche, A. Valeri, T. Mignot and M. Nollmann, *PLoS One*, 2013, **8**, e76268.
3 E. Chung, D. Kim, Y. Cui, Y. H. Kim and P. T. So, *Biophys. J.*, 2007, **93**, 1747–1757.
4 J. Bückers, D. Wildanger, G. Vicidomini, L. Kastrup and S. W. Hell, *Opt. Express*, 2011, **19**, 3130–3143.
5 E. Betzig, G. H. Patterson, R. Sougrat, O. W. Lindwasser, S. Olenych, J. S. Bonifacino, M. W. Davidson, J. L. Schwartz and H. F. Hess, *Science*, 2006, **313**, 1642–1645.
6 L. Schermelleh, P. M. Carlton, S. Haase, L. Shao, L. Winoto, P. Kner, B. Burke, M. C. Cardoso, D. A. Agard, M. G. L. Gustafsson, H. Leonhardt and J. W. Sedat, *Science*, 2008, **320**, 1332–1336.
7 S. Dilipkumar and P. P. Mondal, *Rev. Sci. Instrum.*, 2012, **83**, 123704.
8 N. Stevens, N. O'Connor, H. Vishwasrao, D. Samaroo, E. R. Kandel, D. A. Akins, C. M. Drain and N. J. Turro, *J. Am. Chem. Soc.*, 2008, **130**, 7182–7183.
9 Z. Tian, W. Wu, W. Wan and A. D. Q. Li, *J. Am. Chem. Soc.*, 2008, **131**, 4245–4252.
10 L. Zhu, W. Wu, M. Q. Zhu, J. J. Han, J. K. Hurst and A. D. Q. Li, *J. Am. Chem. Soc.*, 2007, **129**, 3524–3526.
11 F. V. Subach, G. H. Patterson, M. Renz, J. L. Schwartz and V. V. Verkhusha, *J. Am. Chem. Soc.*, 2010, **132**, 6481–6491.
12 B. R. Schroeder, M. Imran Ghare, C. Bhattacharya, R. Paul, Z. Yu, P. A. Zaleski, T. C. Bozeman, M. J. Rishel and S. M. Hecht, *J. Am. Chem. Soc.*, 2014, **136**, 13641–13656.
13 Z. Yu, R. M. Schmaltz, T. C. Bozeman, R. Paul, M. J. Rishel, K. S. Tsosie and S. M. Hecht, *J. Am. Chem. Soc.*, 2013, **135**, 2883–2886.
14 C. Dong, R. Eldawud, L. M. Sargent, M. L. Kashon, D. Lowry, Y. Rojanasakulc and C. Z. Dinu, *Environ. Sci.: Nano*, 2014, **1**, 595–603.
15 K. J. Siegrist, S. H. Reynolds, M. L. Kashon, D. T. Lowry, C. Dong, A. F. Hubbs, S. H. Young, J. L. Salisbury, D. W. Porter, S. A. Benkovic, M. McCawley, M. J. Keane, J. T. Mastovich, K. L. Bunker, L. G. Cena, M. C. Sparrow, J. L. Sturgeon, C. Dinu and L. M. Sargent, *Part. Fibre Toxicol.*, 2014, **11**, 6.
16 K. S. Y. Liu, M. Siebert, S. Mertel, E. Knoche, S. Wegener, C. Wichmann, T. Matkovic, K. Muhammad, H. Depner, C. Mettke, J. Bückers, S. W. Hell, M. Müller, G. W. Davis, D. Schmitz and S. J. Sigrist, *Science*, 2011, **334**, 1565–1569.
17 L. P. Kozak and M. E. Young, *Nat. Med.*, 2012, **18**, 1458–1459.
18 M. Volk, L. Milanesi, J. P. Waltho, C. A. Hunter, S. Dev, D. J. Shaw, G. S. Beddard and G. D. Reid, *Biophys. J.*, 2009, **96**, 322a–323a.
19 P. Ramajo, S. A. Petty and M. Volk, *Chem. Phys.*, 2006, **323**, 11–20.

20 A. Nebenführ, L. A. Gallagher, T. G. Dunahay, J. A. Frohlick, A. M. Mazurkiewicz, J. B. Meehl and L. A. Staehelin, *Plant Physiol.*, 1999, **121**, 1127–1141.
21 P. Kner, B. B. Chhun, E. R. Griffis, L. Winoto and M. G. L. Gustafsson, *Nat. Methods*, 2009, **6**, 339–342.
22 M. R. Verma, K. Rajan and P. P. Mondal, *AIP Adv.*, 2012, **2**, 032174.
23 S. Krobitsch and S. Lindquist, *Proc. Natl. Acad. Sci. U. S. A.*, 2000, **97**, 1589–1594.
24 K. Meiling-Wesse, U. D. Epple, R. Krick, H. Barth, A. Appelles, C. Voss, E. L. Eskelinen and M. Thumm, *J. Biol. Chem.*, 2005, **280**, 33669–33678.
25 C. C. Weihl, *Neurotherapeutics*, 2013, **10**, 383–390.
26 P. P. Mondal and A. Diaspro, *Sci. Rep.*, 2011, **1**, 149.
27 S. Dilipkumar and P. P. Mondal, *Appl. Phys. Lett.*, 2013, **103**, 073702.
28 P. P. Mondal, G. Vicidomini and A. Diaspro, *Appl. Phys. Lett.*, 2008, **92**, 103902.
29 E. Scherzinger, A. Sittler, K. Schweiger, V. Heiser, R. Lurz, R. Hasenbank, G. P. Bates, H. Lehrach and E. E. Wanker, *Proc. Natl. Acad. Sci. U. S. A.*, 1999, **96**, 4604–4609.
30 J. Tyedmers, A. Mogk and B. Bukau, *Nat. Rev. Mol. Cell Biol.*, 2010, **11**, 777–788.
31 E. Teuling, A. Bourgonje, S. Veenje, K. Thijssen, J. de-Boer, J. van der Velde, M. Swertz and E. Nollen, *PLoS Curr.*, 2011, **3**, RRN1255.
32 P. P. Mondal, G. Vicidomini and A. Diaspro, *J. Appl. Phys.*, 2007, **102**, 044701.
33 I. G. Heller, O. D. Sitters, G. Broekmans, C. Farge, W. Menges, W. Wende, S. W. Hell, E. J. G. Peterman and G. J. L. Wuite, *Nat. Methods*, 2013, **10**, 910–916.
34 M. Lakadamyali, H. Babcock, M. Bates, X. Zhuang and J. Lichtman, *PLoS One*, 2012, **7**, e30826.
35 J. Zimmerberg and S. T. Hess, *Cell*, 2011, **146**, 501–503.
36 G. M. P. Van Kempen, L. J. Van Vliet, P. J. Verveer and H. T. M. Van der Voort, *J. Microsc.*, 1997, **185**, 354.
37 T. Ideker, J. Dutkowski and L. Hood, *Cell*, 2011, **144**, 860–863.
38 A. Lorbert, D. M. Blei, R. E. Schapire and P. J. Ramadge, ArXiv e-prints, 2012.